JACS
JOURNAL OF THE AMERICAN CHEMICAL SOCIETY
pubs.acs.org/JACS
Article

Contribution of Nitrogen Vacancies to Ammonia Synthesis over Metal Nitride Catalysts

Tian-Nan Ye,[#] Sang-Won Park,[#] Yangfan Lu,[#] Jiang Li, Masato Sasase, Masaaki Kitano,* and Hideo Hosono*

Cite This: https://dx.doi.org/10.1021/jacs.0c06624

ABSTRACT: Ammonia is one of the most important feedstocks for the production of fertilizer and as a potential energy carrier. Nitride compounds such as LaN have recently attracted considerable attention due to their nitrogen vacancy sites that can activate N_2 for ammonia synthesis. Here, we propose a general rule for the design of nitride-based catalysts for ammonia synthesis, in which the nitrogen vacancy formation energy (E_{NV}) dominates the catalytic performance. The relatively low E_{NV} (ca. 1.3 eV) of CeN means it can serve as an efficient and stable catalyst upon Ni loading. The catalytic activity of Ni/CeN reached 6.5 mmol·g^{-1}·h^{-1} with an effluent NH_3 concentration (E_{NH3}) of 0.45 vol %, reaching the thermodynamic equilibrium (E_{NH3} = 0.45 vol %) at 400 °C and 0.1 MPa, thereby circumventing the bottleneck for N_2 activation on Ni metal with an extremely weak nitrogen binding energy. The activity far exceeds those for other Co- and Ni-based catalysts, and is even comparable to those for Ru-based catalysts. It was determined that CeN itself can produce ammonia without Ni-loading at almost the same activation energy. Kinetic analysis and isotope experiments combined with density functional theory (DFT) calculations indicate that the nitrogen vacancies in CeN can activate both N_2 and H_2 during the reaction, which accounts for the much higher catalytic performance than other reported nonloaded catalysts for ammonia synthesis.

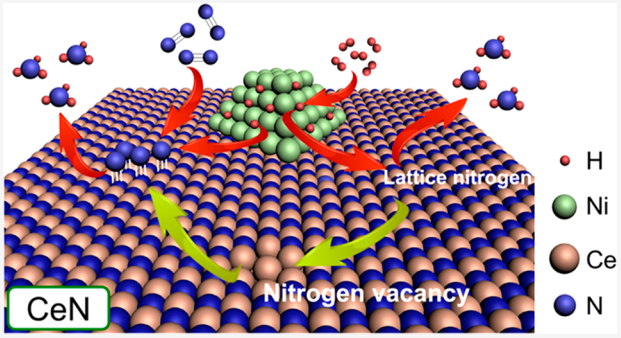

INTRODUCTION

Ammonia is important for the production of chemicals and fertilizer worldwide.[1] N_2 activation to form ammonia (NH_3) is the general route for ammonia production, which requires the large N≡N bond energy (945 kJ·mol^{-1}) to be overcome.[2,3] The major milestone for industrial ammonia production was the development of the Haber−Bosch process. It was demonstrated that Fe-based catalysts could generate NH_3 from N_2 and H_2 molecules under high temperature (400−600 °C) and high pressure (20−40 MPa) conditions.[4,5] Although electrochemical and photocatalytic approaches have been attempted under milder conditions,[6−10] the efficiency and production scale have been far from industrial requirements, which has led to the preference of the traditional thermal catalytic process for large scale NH_3 production. There is thus a high demand to develop more efficient substitutes as industrial catalysts, and as such, further fundamental scientific research has been undertaken.

The surface properties of heterogeneous catalysts are critical for catalytic performance, and the introduction of surface defect sites has emerged as an effective strategy to achieve high activity for various chemical reactions.[11−13] For instance, oxygen vacancies are considered to participate in chemical reactions such as the oxidation of aromatic hydrocarbons and CO over metal oxides such as V_2O_5 and CeO_2, which are interpreted within the Mars−van Krevelen mechanism.[14−17] This mechanism was further extended to ammonia synthesis recently using oxyhydride and oxynitride based materials, in which incorporated N^{3-} and/or H^- ions play a vital role for ammonia production.[18−20] For example, the transition metal (TM)-loaded 12CaO·7Al_2O_3 electride and $Ca(NH_2)_2$ exhibit excellent catalytic activity for ammonia synthesis by the presence of anionic electrons and incorporated H^- ions.[21−26] TM-loaded metal hydrides (AH_x, A = Li, Na, K, Ba, Ca) can extract dissociated N from TMs to form metal-imide species, which then undergo hydrogenation to the final NH_3 product.[27−29] Although high catalytic performance has been achieved, these efficient support materials are still dependent on the loading of active metals. Some perovskite materials, such as $BaCeO_{3-x}N_yH_z$ and $BaTiO_{2.5}H_{0.5}$, also generate ammonia, even without TM loading.[30−33] For each case, the

Received: June 19, 2020

https://dx.doi.org/10.1021/jacs.0c06624
J. Am. Chem. Soc. XXXX, XXX, XXX−XXX

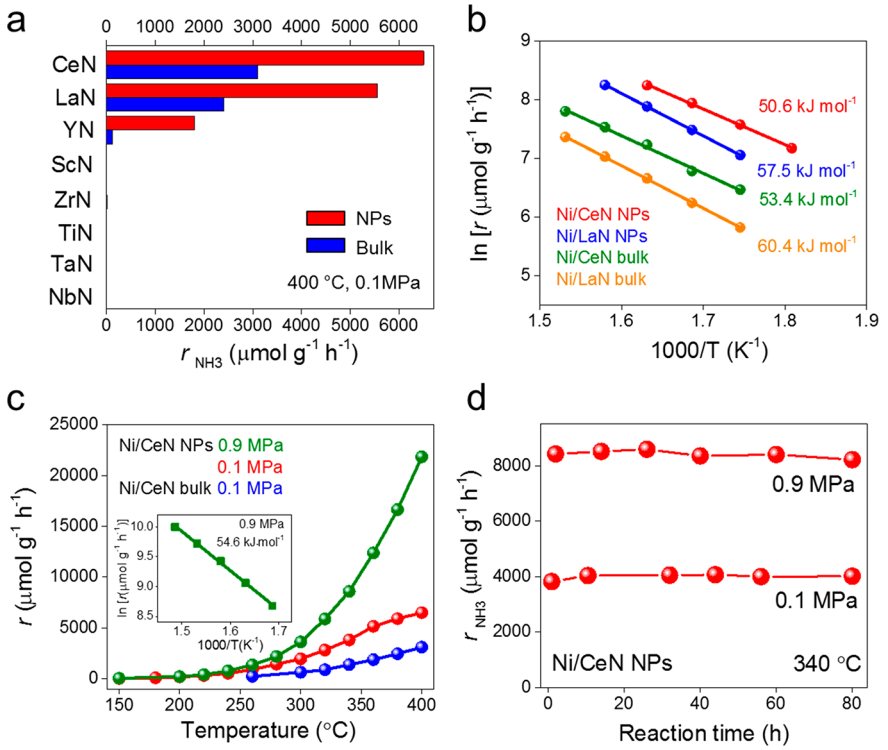

Figure 1. Catalytic activity of Ni-loaded different nitrides. (a) Catalytic activity (blue, bulk; red, nanoparticles (NPs)) for ammonia synthesis over various nitride-supported Ni catalysts. (b) Arrhenius plots for ammonia synthesis over Ni/CeN NPs, Ni/LaN NPs, Ni/CeN bulk, and Ni/LaN bulk catalysts at 0.1 MPa. (c) Temperature dependence of ammonia synthesis activity over Ni/CeN NPs and Ni/CeN bulk at 0.1 and 0.9 MPa. The inset of (c) shows an Arrhenius plot for ammonia synthesis over Ni/CeN NPs at 0.9 MPa. (d) Time course of ammonia synthesis over the Ni/CeN NP catalyst at 0.1 and 0.9 MPa. (Reaction conditions: 0.1 g catalyst, N_2:H_2 = 15:45 mL min^{-1}, 150−400 °C, 0.1 and 0.9 MPa).

formation of nitride-hydride surface species significantly promotes the catalytic performance of TMs. Accordingly, a support material with high nitrogen affinity is considered to enhance the catalytic performance of the TMs.

In this context, we recently demonstrated that a (LaN-Ni) catalyst with dual active sites could separately activate H_2 and N_2 molecules, and successfully overcome the scaling relationship that has restricted the use of Ni-based catalysts for ammonia synthesis due to the extremely weak nitrogen binding energy of Ni.[34] One of the highlighted points of LaN is its low nitrogen vacancy formation energy (E_{NV}). It was demonstrated that the lattice N of LaN directly reacts with dissociated hydrogen (H*) from the Ni surface to generate NH_3 and N vacancies. N_2 molecules are subsequently adsorbed and activated at the N vacancy sites, and continuously react with H* to realize a stable catalytic cycle. The role of nitride supports and their N vacancies has therefore inspired us to consider E_{NV} as an important factor, and a general rule for the design of Ni-based catalysts for ammonia synthesis.

In the present study, the correlation of E_{NV} over various nitride supported Ni catalysts for ammonia synthesis was clarified first. Among these tested nitrides, CeN showed the highest activity with Ni loading, which is characterized by a lower E_{NV} and a suppressed activation barrier toward ammonia synthesis. CeN itself also serves as a stable catalyst for ammonia synthesis, even without TMs-loading. Kinetic analysis and isotope experiments indicate that the N vacancies in CeN contribute to the activation of both N_2 and H_2 molecules. The experimental data obtained are consistent with the theoretical calculations, which indicate that the ease of N vacancy formation determines the catalytic activity for ammonia synthesis over nitride compounds, with and without Ni loading.

RESULTS AND DISCUSSION

To test the effect of the nitride support on the catalytic performance of Ni, rare-earth metals (*Re*) based nitrides *Re*N (*Re* = Ce, La, Y, and Sc) and early transition metals (*Et*) based nitrides *Et*N (*Et* = Zr, Ti, Ta, and Nb) were employed as supports with the same amount of Ni loading (ca. 5 wt % for bulk, ca. 10 wt % for nanoparticles (NPs)) (Figures S1−S3). Figure 1a compares the activities of Ni/*Re*N and Ni/*Et*N catalysts at 400 °C and at a reactant gas (H_2:N_2 = 3:1) pressure of 0.1 MPa. Ni/*Re*N effectively produced ammonia, while the activities of Ni/*Et*N were below the detection limit. In particular, Ni/CeN exhibited the highest activities, which were as high as 3100 and 6500 μmol·g^{-1}·h^{-1} for the bulk and NPs, respectively. In the turnover frequency (TOF) calculation, the concentration of surface nitrogen vacancies (V_N) used was 3.9×10^{14} cm^{-2} from the amount of top layer lattice N of CeN, which are the active sites of the Ni/CeN catalyst (details for the active sites are discussed later). The TOF of Ni/CeN was estimated to be 0.064 s^{-1}. The catalytic activities and TOF value far exceed those of the other reported Ni- and Co-based catalysts, and are even comparable to those of noble metal catalysts, such as the Ru catalysts (Tables S1, S2).[24,28,35−40] The activities of the Ni/*Re*N catalysts are ranked in the order of Ni/CeN > Ni/LaN > Ni/YN > Ni/ScN for both the bulk and NP samples (as shown by the red and blue bars in Figure 1a). Considering the similar specific surface areas and Ni particle sizes of these Ni/*Re*N samples (Figure S4), this order for the capability to promote the reaction is

https://dx.doi.org/10.1021/jacs.0c06624
J. Am. Chem. Soc. XXXX, XXX, XXX−XXX

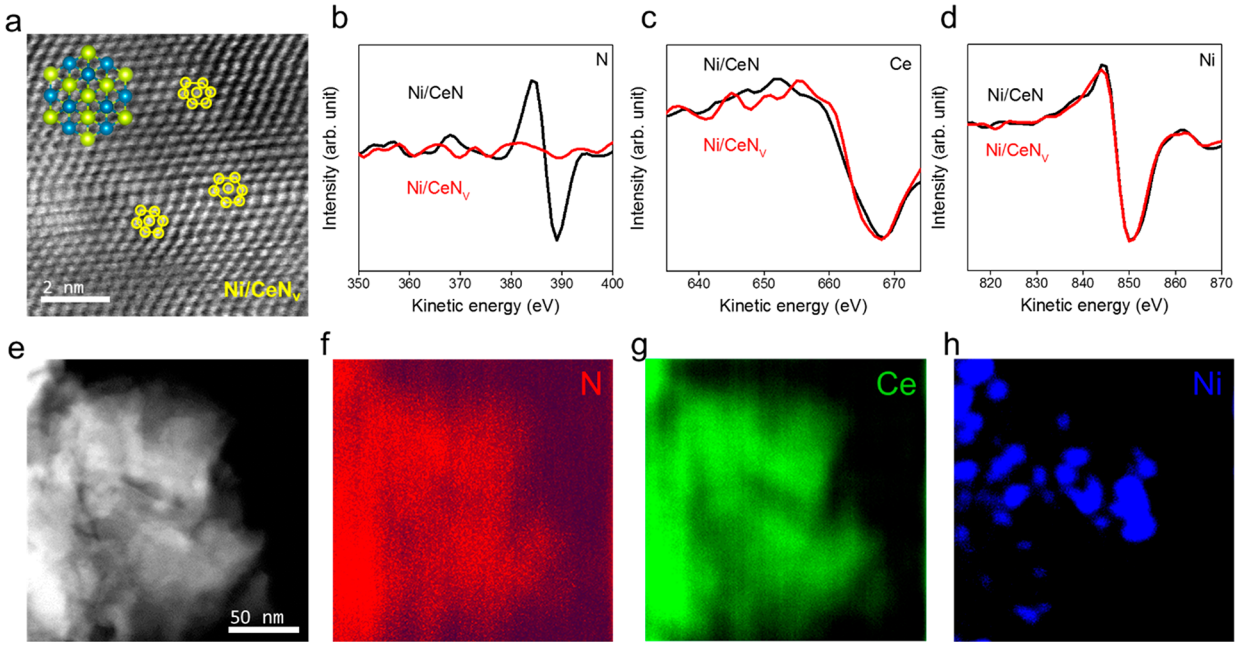

Figure 2. Characterization of Ni/CeN. (a) HAADF-STEM image of CeN regions in N-deficient Ni/CeN$_v$ along the [111] direction. The inset of (a) shows the corresponding crystal structure of CeN along the [111] direction. Ce and N atoms are represented as yellow and blue balls, respectively. (b–d) AES spectra of fresh and N-deficient Ni/CeN$_v$. (e) HAADF-STEM image and (f–h) EDX mapping results for N, Ce, and Ni in the used Ni/CeN catalyst.

considered to originate from the role of the nitride support rather than that of the Ni sites. The apparent activation energies (E_a) of the Ni/CeN and Ni/LaN catalysts are close to ca. 60 kJ·mol^{-1} in the temperature range of 280–380 °C at 0.1 MPa (Figure 1b). The Ni/YN bulk catalyst shows a higher E_a (ca. 90 kJ·mol^{-1}) in the relative high temperature range of 400–500 °C at 0.1 MPa (Figure S5), which suggests that the reaction mechanism over the Ni/CeN and Ni/LaN catalysts is similar, i.e., H_2 and N_2 molecules are separately activated on the loaded Ni and surface V_N sites of the *Re*N support, which was confirmed through an isotope experiment using $^{15}N_2$ and H_2 and the isotopic exchange reaction between $^{14}N_2$ and $^{15}N_2$ (Figure S6, S7).[34]

As the most active sample, the generation of surface V_N on the CeN support was further confirmed by high-angle annular dark-field scanning transmission electron microscopy (HAADF-STEM) along the [111] direction. Local distortion could be identified after the treatment of Ni/CeN in a H_2 atmosphere at 400 °C, which suggests the dislocation of Ce atoms due to the formation of a substantial amount of N defects (Figure 2a). To further confirm the generation of N defects, Auger electron spectroscopy (AES) was performed to investigate the surface composition. The depth dependence of the N peak (ca. 387 eV) from the AES spectra show that N defects are more likely to be generated on the CeN surface (Figures 2b and S8). Figure 2b shows that fresh CeN has a stronger N peak than that after H_2 treatment, while the Ce and Ni peaks remains unchanged (Figure 2c,d). Consideration of both the results of local distortion and reduced N AES peaks suggests that a substantial amount of N defects were formed on the Ni/CeN surface by H_2 treatment. Energy-dispersive X-ray spectroscopy (EDX) mapping of the Ni/CeN sample collected after reaction (Figure 2e–h) revealed that Ce and N are uniformly dispersed on CeN. The mean Ni particle size was estimated to be ca. 30 nm, which is consistent with scanning electron microscopy (SEM) observations (Figure S4a).

To further understand the degree of the metal–support interaction, we performed the PDOS calculations of Ni_8 cluster on nitrogen vacancy-free CeN surface ($Ni_8/Ce_{48}N_{48}$), Ni_8 cluster on V_N existed CeN surface ($Ni_8/Ce_{48}N_{47}$) and pure V_N existed CeN surface ($Ce_{48}N_{47}$). As shown in Figure S9, in both Ni loaded cases, the density of states near Fermi level was mainly contributed by the Ni 3*d* orbitals. Compared with the PDOS of $Ni_8/Ce_{48}N_{48}$, $Ni_8/Ce_{48}N_{47}$ gave a significant shift due to the electron doping, associated with the generation of N vacancy. Therefore, the electronic energy region of the Fermi level shifting is dominated by Ni 3*d* orbitals, and thus doped electrons should be transferred from the V_N to the Ni sites. While CeN support and Ni metal do not form ternary compounds, Ni_8 cluster can be strongly interacted with CeN through such electron transfer during the catalytic cycles since each of them was electronically connected. The orbital hybridization between Ni_8 cluster and N 2*p* orbitals is also an important interaction between Ni and CeN support. As shown in Figure S10, Ni[1] 3*d* orbitals hybridize with the nearest N[2] 2*p* orbitals, and exhibit a substantial overlapping of PDOS at around $-4 < E - E_F < -2$ eV. Such contribution cannot be seen for the second nearest N[1] at the corresponding energy range. This effect stabilizes the loaded Ni_8 cluster as well, and the stabilization energy was calculated to be −8.8 eV per Ni_8 cluster.

The reaction orders of the Ni/CeN catalyst were estimated to be N_2 (α) = 1.2, H_2 (β) = 1.6, and NH_3 (γ) = −1.4, which would result in a desirable high-pressure effect (Table S3). The reaction rates increase monotonically with the reactant gas pressure and no hydrogen poisoning was observed (Figure 1c and S11). It should be noted that E_a for Ni/CeN NPs was measured to be 54.6 kJ·mol^{-1} under 0.9 MPa (Figure 1c inset), which is close to that under 0.1 MPa (Figure 1b) and indicates the reaction mechanism remains unchanged under high-pressure conditions. The catalyst produced ammonia continuously without degradation for 80 h at 340 °C and at both

https://dx.doi.org/10.1021/jacs.0c06624
J. Am. Chem. Soc. XXXX, XXX, XXX–XXX

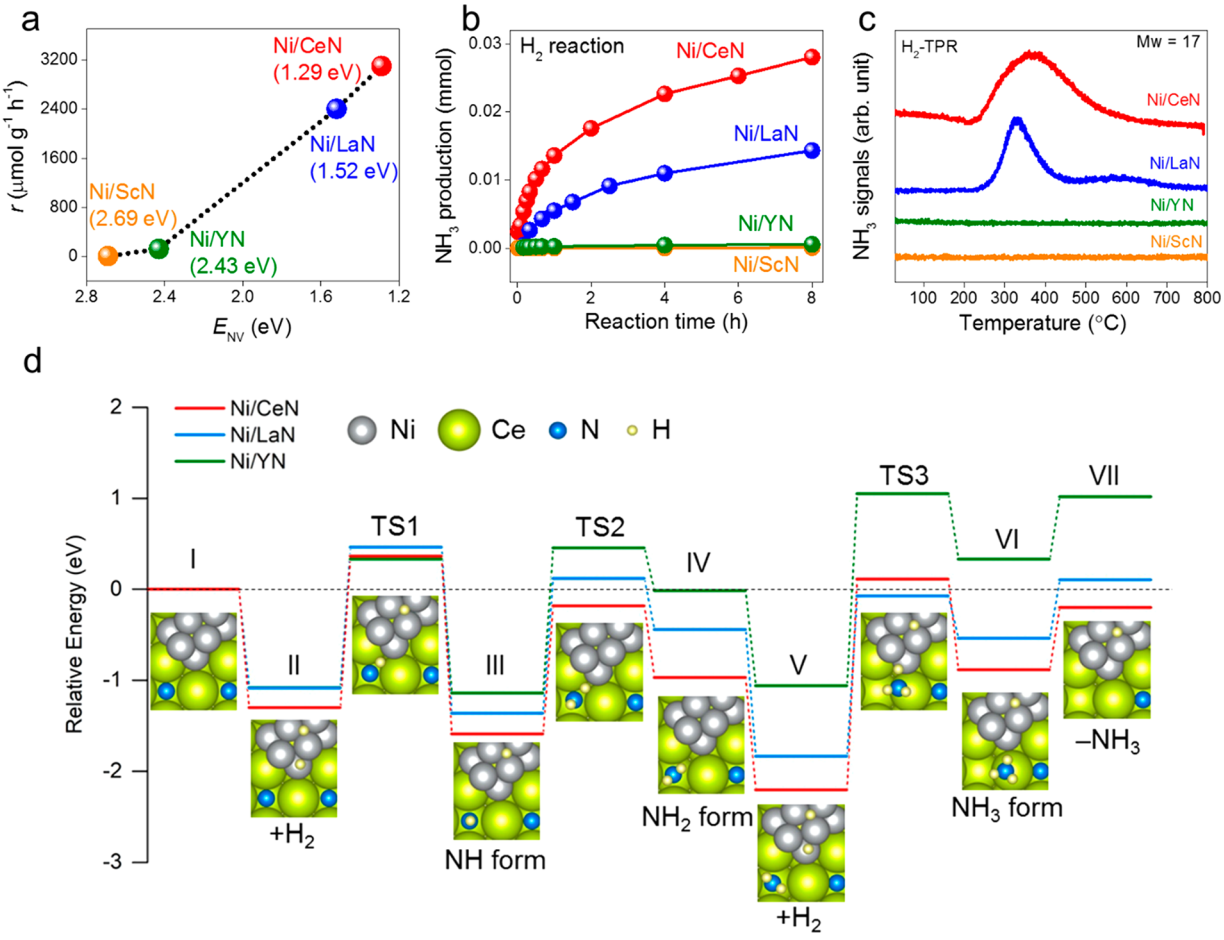

Figure 3. Comparison of ammonia production, H_2-TPR results and DFT studies over various nitride-supported Ni catalysts. (a) Ammonia synthesis activity and N vacancy formation energies (E_{NV}) over various nitride-supported Ni catalysts. (b) Cumulative amounts of NH_3 generated over various nitride bulk-supported Ni catalysts as a function of time using pure H_2 gas supply at 400 °C. (c) H_2-TPR profiles for various nitride-supported Ni catalysts. (d) Energy profiles from DFT studies of the reaction path for ammonia synthesis with various nitride-supported Ni catalysts.

0.1 and 0.9 MPa, which confirmed excellent stability (Figure 1d).

To determine the origin of the different catalytic performance among the Ni/*Re*N catalysts with similar surface area and particle size (Figure S4), DFT calculations were conducted and nitrogen vacancy formation energies (E_{NV}) were calculated to be Ni/CeN (1.29 eV) < Ni/LaN (1.52 eV) < Ni/YN (2.43 eV) < Ni/ScN (2.69 eV), which indicates that $N_{lattice}$ in Ni/CeN are more easily removed than $N_{lattice}$ in Ni/LaN, Ni/YN, and Ni/ScN (Figure 3a). Accordingly, the measurements of $N_{lattice}$ removal from these Ni-loaded nitride catalysts reveal a higher NH_3 production rate over Ni/CeN, with the lowest E_{NV} among these Ni/*Re*N catalysts (Figure 3b). Furthermore, H_2-temperature-programmed reduction (H_2-TPR) data showed finite NH_3 desorption from Ni/CeN and Ni/LaN (Figure 3c). The NH_3 desorption temperature of CeN (220 °C) is slightly lower than that of LaN (250 °C), which is consistent with the results of the pure H_2 supply experiment (Figure 3b). In contrast, negligible NH_3 was detected over Ni/YN and Ni/ScN (Figure 3c). These experimental results indicate that the removal of $N_{lattice}$ from Ni/CeN by H_2 proceeds more easily than from Ni/LaN, Ni/YN, and Ni/ScN, which is consistent with the different E_{NV} values (Figure 3a). As we reported for Ni/LaN, the combined process of H* and $N_{lattice}$ in LaN is the rate-determining step (RDS) for the ammonia synthesis reaction.[34] Here, the reaction barrier for $N_{lattice}$ hydrogenation over Ni/*Re*N (*Re* = Ce, La, and Y) catalysts was also calculated. The energy profiles of the intermediate structures and transition states (TSs) as the key elementary steps are shown in Figure 3d and Table S4–S6. The TS energy of the $N_{lattice}$ hydrogenation step (TS1) is the highest among all the reaction steps for the Ni/LaN and Ni/CeN catalysts. Therefore, the overall activation barrier for NH_3 formation on Ni/CeN is ca. 0.37 eV, which is slightly lower than that on Ni/LaN (ca. 0.46 eV), and indicates that $N_{lattice}$ in CeN is more easily hydrogenated by H* than that in LaN, which is in good agreement with the distinction of the experimentally obtained E_a (Figure 1b). However, in the case of Ni/YN, the overall activation barrier comes from the hydrogenation of NH_2 species (TS3) with an exceptionally large barrier of ca. 1.05 eV. This could be ascribed to the relatively large E_{NV} of Ni/YN (Figure 3a), which makes it difficult to remove the $N_{lattice}$ from the YN lattice and is consistent with the experimentally obtained E_a of ca. 0.95 eV (ca. 91.5 kJ·mol^{-1}) with Ni/YN (Figure S5). Moreover, from the final the energy state in step VII (Figure 3d), V_N on Ni/CeN are much more stable than those on Ni/LaN and Ni/YN, which is also in good agreement with the distinction in the E_a (Figure 1b) and E_{NV} (Figure 3a). We also calculated the N_2 adsorption energy (E_{N2}) into the V_N of these Ni-loaded nitrides to be Ni/CeN

https://dx.doi.org/10.1021/jacs.0c06624
J. Am. Chem. Soc. XXXX, XXX, XXX−XXX

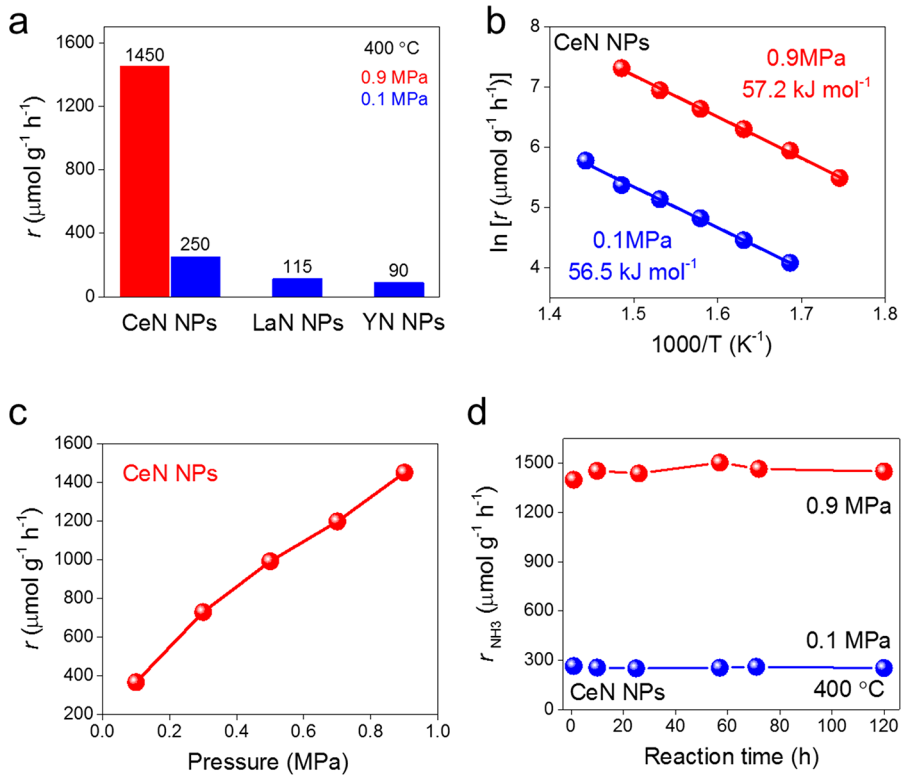

Figure 4. Catalytic performance for ammonia synthesis over various nonloaded nitride catalysts. (a) Catalytic activity (blue, 0.1 MPa; red, 0.9 MPa) for ammonia synthesis over pure CeN, LaN, and YN NPs. (b) Arrhenius plots for ammonia synthesis over pure CeN NPs at 0.1 and 0.9 MPa. (c) Pressure dependence of ammonia synthesis activity over pure CeN NPs. (d) Time course for ammonia synthesis over pure CeN NPs at 0.1 and 0.9 MPa. (Reaction conditions: 0.1 g catalyst, N_2:H_2 = 15:45 mL min^{-1}, 300−400 °C, 0.1−0.9 MPa).

(E_{N2} = −1.21 eV), Ni/LaN (E_{N2} = −1.03 eV), and Ni/YN (E_{N2} = −1.56 eV). Accordingly, the N≡N bond lengths were increased to 1.25 Å for Ni/CeN, 1.26 Å, for Ni/LaN and 1.32 Å for Ni/YN, which suggests that the removal of the top N (end-on adsorbed N_2) proceeds more easily from Ni/YN than from Ni/CeN and Ni/LaN. However, the reaction rate over Ni/YN is much lower than that over Ni/CeN and Ni/LaN, which indicates that down N (equal to $N_{lattice}$) hydrogenation controls the reaction rate; this is strongly related to the E_{NV} we have proposed (Figure 3a). Therefore, the calculation results presented here indicate that the RDS for ammonia synthesis over the Ni/*Re*N catalysts is not N_2 dissociation, but one of the $N_{lattice}$ hydrogenation steps. The reaction barrier for $N_{lattice}$ hydrogenation (RDS) over Ni/CeN is obviously lower than those over Ni/LaN and Ni/YN because of the relatively low E_{NV} (ca. 1.3 eV), which results in the significantly higher catalytic activity of Ni/CeN (Figure 1a). Figure S12 shows the comparison of NH_3 desorption from Ni/CeN bulk and NPs during H_2-TPR. The NH_3 desorption reflects the reaction of hydrogen with lattice nitrogen on Ni/CeN catalysts and simultaneous V_N formation. The integrated peak area of the Ni/CeN NPs for NH_3 desorption is almost twice that of Ni/CeN bulk sample. Thus, the number of active sites on Ni/CeN NPs is almost double that of Ni/CeN bulk catalyst, which is consistent with the difference in the catalytic activities of these two catalysts (Figure 1a). This result further supports our proposed mechanism.

In the cases of Ni/*Et*N, the E_{NV} values for Ni/ZrN and Ni/NbN were calculated to be 3.36 and 1.84 eV, respectively. Here, we consider that the negligible catalytic performance could be ascribed to the reported larger nitrogen vacancy formation energy compared with that for cation vacancies,[41] which makes it almost impossible to remove $N_{lattice}$ from these compounds, and this was also confirmed by the absence of NH_3 in the H_2-TPR results for the Ni/*Et*N catalysts with similar specific surface areas and Ni particle sizes (Figure S13, S14). All of these computational and experimental results indicate that the catalytic activities of Ni/*Re*N (*Re* = Ce, La, and Y) are closely related to E_{NV}, which demonstrates the importance of V_N in various nitrides for N_2 activation and hydrogenation toward Ni loaded catalysts for ammonia synthesis.

Overall, the Ni/CeN catalyst was demonstrated to be the most efficient Ni-based catalyst for ammonia synthesis reported to date. During the reaction, dissociated H* from the Ni surface can directly react with $N_{lattice}$ of CeN to generate NH_3 and nitrogen vacancies. N_2 molecules are subsequently activated at the defect sites and again react with H* to realize a stable catalytic cycle. Here, we consider whether nitrogen defects can also activate H_2 molecules, i.e., whether CeN itself can also act as a stable catalyst for ammonia synthesis. Given the much higher surface areas of the NP samples among pure CeN, LaN, and YN, the catalytic performance for ammonia synthesis over pure NP catalysts is shown in Figure 4a. Pure CeN NPs exhibited catalytic activities of 250 and 1450 $\mu mol \cdot g^{-1} \cdot h^{-1}$ at 0.1 and 0.9 MPa (400 °C, WHSV: 36 000 $mL \cdot g^{-1} \cdot h^{-1}$), respectively, which are 2 times higher than those with pure LaN and YN NPs. To the best of our knowledge, the catalytic activity of pure CeN NPs is superior to those of other reported non-TM-loaded catalysts, such as $BaCeO_{3-x}N_yH_z$ (430 $\mu mol \cdot g^{-1} \cdot h^{-1}$, 400 °C, 0.9 MPa, WHSV: 36 000 $mL \cdot g^{-1} \cdot h^{-1}$) and $BaTiO_{2.5}H_{0.5}$ (700 $\mu mol \cdot g^{-1} \cdot h^{-1}$, 400 °C, 5 MPa,

https://dx.doi.org/10.1021/jacs.0c06624
J. Am. Chem. Soc. XXXX, XXX, XXX−XXX

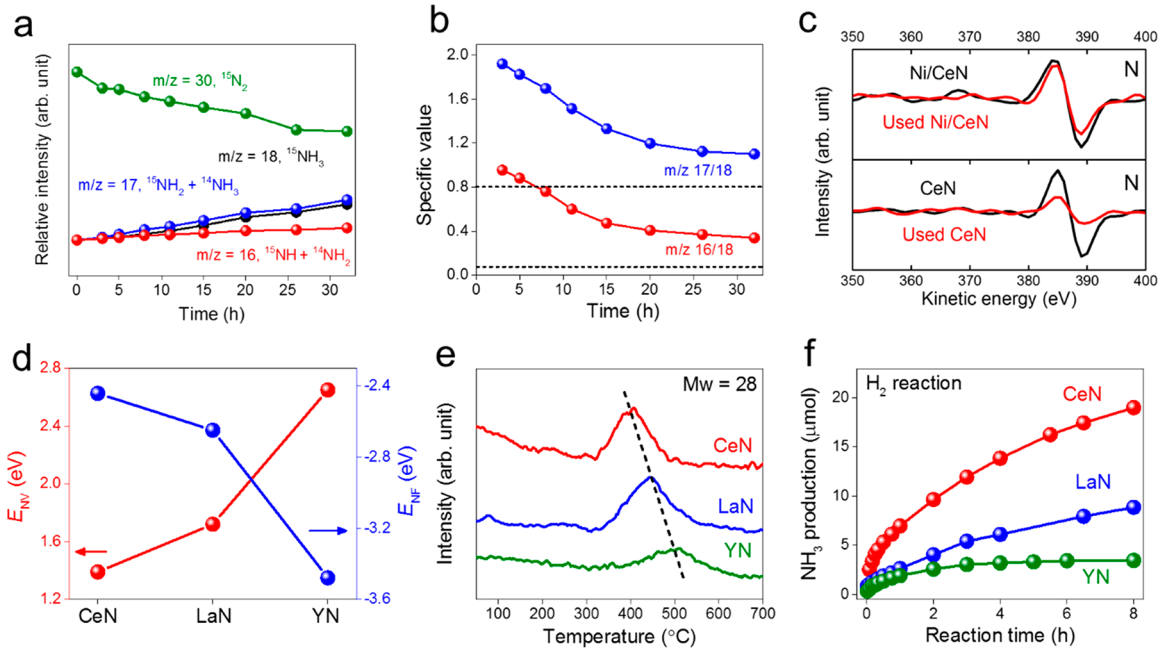

Figure 5. Characterization and DFT calculations of various nitrides. (a) Reaction time profiles for NH_3 synthesis from $^{15}N_2$ and H_2 over fresh CeN. (b) Reaction time profiles for the ratio changes of 17/18 and 16/18 according to (a), where in mass spectrometry, NH_2/NH_3 = 0.8 and NH/NH_3 = 0.075. (c) AES spectra N signals for fresh and used Ni/CeN, and pure CeN catalysts. (d) N vacancy formation energies (E_{NV}) and nitride formation energies (E_{NF}) for pure CeN, LaN and YN catalysts. (e) TPD profiles for ammonia synthesis over used CeN, LaN, and YN NPs catalysts. (f) Cumulative amounts of NH_3 generated over pure CeN, LaN, and YN NP catalysts as a function of time using pure H_2 gas supply at 400 °C.

WHSV: 54 000 mL·g^{-1}·h^{-1}), as shown in Figure S15.[30,32] The E_a for the pure CeN NPs were estimated to be 56.5 and 57.2 kJ·mol^{-1} at 0.1 and 0.9 MPa (Figure 4b), which were comparable to those for the Ni/CeN catalyst (Figure 1b), but smaller than those for other reported non-TM-loaded catalysts (70−80 kJ·mol^{-1}) (Figure S15). The reaction orders with respect to N_2, H_2, and NH_3 were measured to be 1.0, 1.3, and −1.6 (Figure S16 and Table S3), similar to those of Ni/CeN catalyst, indicating a similar reaction mechanism which will be discussed later. A positive pressure effect, almost 6-fold enhancement of the reaction rate, was achieved when the pressure was increased from 0.1 to 0.9 MPa (Figure 4c). The crystal structure and the initial ammonia synthesis rates were maintained after 120 h under both ambient and high pressure conditions (Figure 4d and S17), and the total amount of generated ammonia reached 17.4 mmol, which was more than 26 times the total nitrogen content in the CeN catalyst (0.65 mmol). This result indicates that the produced ammonia is not derived from the decomposition of CeN, but from the catalytic cycle.

To further clarify the mechanism, the isotopic effect was measured using $^{15}N_2$ and H_2 over the pure CeN NP catalyst. Figure 5a shows the changes in intensity for mass numbers as a function of time. Ammonia isotopomer-related species with the mass signals of m/z = 16 (^{15}NH or $^{14}NH_2$), 17 ($^{15}NH_2$ or $^{14}NH_3$), 18 ($^{15}NH_3$), and 30 ($^{15}N_2$) were all detected. After the introduction of isotope gas $^{15}N_2$ and H_2, the signals measured for the intensity ratios of m/z 17/18 and 16/18 were larger than the theoretical values of 0.8 (m/z 17/18) and 0.075 (m/z 16/18), which indicated the generation of both $^{14}NH_3$ and $^{15}NH_3$ (Figure 5b). These results clearly indicate that the lattice ^{14}N of CeN participate in the formation of ammonia, which is consistent with the case for Ni/CeN (Figure S6).

These results raise the following question. How can H_2 molecules be activated and dissociated to form reactive hydrogen species? To address this point, the change of the surface composition was estimated from AES measurements (Figures 5c and S18). The variation in the surface composition of Ni/CeN shows that the N peak (ca. 387 eV) remains largely unchanged after reaction, which indicates that the in situ generated surface N vacancies are readily replenished by gas-phase N_2 molecules during ammonia synthesis. Figure S19 shows the calculated adsorption energies of H_2 on the Ni surface and N vacancies are −1.30 and −0.62 eV, respectively, which indicates that H_2 is more likely to be adsorbed on the Ni surface than on the N vacancies of CeN. Given the extreme weak nitrogen adsorption energy of Ni, the N_2 molecules tend to occupy the surface V_N sites with an adsorption energy of −1.21 eV (Figure S19c), which is consistent with the unchanged surface N content indicated by the AES spectra (Figure 5c). In contrast, the surface N content of pure CeN decreased significantly after reaction (Figure 5c), which is ascribed to the competition between H_2 and N_2 molecules to occupy the surface V_N sites. Accordingly, ca. 0.14 hydrogen atoms per formula unit are desorbed from the used CeN catalyst above ca. 250 °C (Figure S20). Also, no amide (NH_2^-) and imide (NH^{2-}) species could be confirmed in Raman spectra the used CeN catalyst (Figure S21). In combination with the AES surface composition analysis and the large amount of H desorption from the TPD measurements, it is reasonable to deduce that the surface V_N sites of pure CeN are mainly occupied by hydrogen species. However, unlike other Ce-based oxide catalysts, H_2 molecules dissociate homolytically and form H^- ions at the V_N sites of CeN, which is evidenced by Bader charge analysis (−0.7 for each dissociated H atom).[30] This large amount of H^- ions that occupy V_N sites then participate in the formation of ammonia.

https://dx.doi.org/10.1021/jacs.0c06624
J. Am. Chem. Soc. XXXX, XXX, XXX−XXX

In the Ni/*Re*N catalyst, E_{NV} determines the catalytic performance for ammonia synthesis upon Ni. The comparable E_a (ca. 60 kJ·mol^{-1}) of pure CeN (Figure 4b) indicates a similar reaction mechanism is valid for Ni/CeN. Here, the hydrogenation process of $N_{lattice}$ in pure CeN was also investigated using DFT calculations (Figure S22 and Table S7). The H_2 molecules can be activated and dissociated on the V_N sites of CeN because of the negligible energy barriers (I → II, IV → V). The surface $N_{lattice}$ reacts step-by-step with H* formed from the nearby V_N sites. After hydrogenation of the surface $N_{lattice}$ by two H*, NH_2 is ejected from the lattice by a dissociated H* by an energy-favored state (step VI). The final hydrogenation step of NH_2 with the dissociated H* creates an overall energy barrier of 0.64 eV for the entire reaction (VI → VII). The calculated reaction paths over pure CeN are slightly different from those over the Ni/CeN catalyst because the overall energy barrier originates from the different hydrogenation steps (Figure 3d). The relatively lower catalytic activity of pure CeN than the Ni-loaded catalyst may be ascribed to the large number of H_2 molecules that occupy the surface V_N sites, which inhibits the adsorption and activation of N_2 molecules (Figure 5c). Here, E_{NV} was also calculated for pure CeN, LaN, and YN in the following order: CeN (1.39 eV) < LaN (1.72 eV) < YN (2.65 eV), which indicates that $N_{lattice}$ is more easily removed from CeN than from LaN and YN (Figure 5d).

The order determined for the nitride formation energy (E_{NF}) was YN (−3.48 eV) < LaN (−2.65 eV) < CeN (−2.44 eV), which indicates the thermodynamic stability of YN is much higher than that for LaN and CeN, and that the most active $N_{lattice}$ is that in CeN, which is consistent with the calculated E_{NV}. Accordingly, N_2 desorption from the used CeN catalyst occurs in a lower temperature range than that from LaN and YN (Figure 5e). To further investigate this relationship with ammonia generation, NH_3 production was investigated using each catalyst under a pure H_2 gas supply (Figure 5f).The NH_3 production over CeN was higher than that over LaN and YN in the following order: YN < LaN < CeN. Therefore, the ease of N vacancy formation also determines the ammonia synthesis reaction over pure nitride compounds without Ni.

■ CONCLUSION

The present work demonstrates that rare earth metal nitrides such as CeN, LaN, and YN can act as efficient supports and/or catalysts for ammonia synthesis, in which nitrogen vacancy formation has a strong effect on the catalytic performance. In the case of Ni-loaded nitrides, H_2 and N_2 are separately activated at Ni metal and V_N sites, respectively. Without Ni loading, V_N sites can activate both H_2 and N_2 simultaneously for stable ammonia production. Due to the relative low E_{NV} (ca. 1.3 eV), CeN itself and with Ni loading were demonstrated to be the most efficient and stable catalyst for ammonia synthesis among the different nitride catalysts investigated. Understanding the role of nitrides may shed light on the design and development of efficient early transition metal based heterogeneous catalysts for other chemical processes.

■ EXPERIMENTAL SECTION

Sample Preparation. CeH_3 and LaH_3 bulk samples were prepared by the treatment of Ce and La chips (99.99%, Kojundo Chemical Lab. Co.) in a 1.5 MPa H_2 atmosphere at room temperature for 2 h. The corresponding CeN and LaN bulk samples were then synthesized by heating CeH_3 and LaH_3 powders at 600 °C under a N_2 gas flow for 6 h. YH_3 and ScH_2 bulk powders were prepared by reacting Y and Sc chips (99.99%, Kojundo Chemical Lab. Co.) in a 1.5 MPa H_2 atmosphere at 400 °C for 4 h. YN and ScN bulk samples were synthesized by heating bulk YH_3 and ScH_2 at 800 and 1000 °C, respectively, under a N_2 flow gas for 24 h. CeH_3, LaH_3, and YH_3 NPs were obtained by an Ar/H_2 arc evaporation method.[42] CeN and LaN NPs were prepared by heating CeH_3 and LaH_3 NPs at 400 °C under a N_2 gas flow for 48 h. YN NPs were synthesized by the heat treatment of YH_3 NPs at 700 °C under a N_2 gas flow for 24 h. Other nitride materials, such as ZrN, TiN, TaN, and NbN, were obtained as commercially available products. For Ni loading, nickelocene ($Ni(C_5H_5)_2$) was used as a Ni precursor, which was mixed with various supports in an agate mortar within an Ar-filled glovebox. The mixture was then heated at 250 °C under a H_2 gas flow for 1.5 h. The nitrides are moisture sensitive; therefore, all of the catalyst preparation procedures were performed in an Ar-filled glovebox.

Catalytic Reaction. Catalytic reactions were conducted in a fixed-bed flow system with a flow of H_2 (>99.99999%) and N_2 (>99.99995%) with a H_2/N_2 flow ratio of 3. The concentration of ammonia in the effluent stream from the catalyst bed (0.1 g) was tested under steady-state conditions at a gas flow rate of 60 mL·min^{-1} in the temperature range of 150−400 °C and under pressure in the range of 0.1−0.9 MPa. The reaction temperature errors were minimized by directly placing a thermocouple into the catalyst in the fixed-bed flow reactor. The ammonia produced was dissolved in 5 mM sulfuric acid solution and the amount of NH_4^+ ions in the solution was identified using ion chromatography (Prominence, Shimadzu) with an electrical conductivity detector. All kinetic results were performed far from equilibrium limitations. The reaction orders with respect to N_2 and H_2 were determined with Ar gas as a diluent to ensure a total flow of 60 mL·min^{-1} when changing the flow rate of N_2 and H_2 at 340 °C and 0.1 MPa.

The ammonia synthesis reaction can be described as shown in eq 1:

$$1/2N_2 + 3/2H_2 \rightarrow NH_3 \quad (1)$$

Then, the effluent NH_3 concentration can be calculated from the reaction rate r_0 (eqs 2−4):

$$Q_{NH3} = r_0 \cdot V_m \cdot m_{cat} \quad (2)$$

$$Q_{total} = Q_{N2} - 1/2Q_{NH3} + Q_{H2} - 3/2Q_{NH3} + Q_{NH3} = Q_{N2} + Q_{H2} - Q_{NH3} \quad (3)$$

$$E_{NH3} = Q_{NH3}/Q_{total} \quad (4)$$

where r_0 is the reaction rate, V_m is the molar volume, m_{cat} is the weight of catalyst, Q_{N2}, Q_{H2}, and Q_{NH3} are the volume flow rates of the feed and product gas, respectively, and E_{NH3} is the effluent NH_3 concentration. Here, thermodynamic limits of effluent NH_3 concentration at 400 °C and under 0.1 MPa is 0.45 vol %.

For calculation of the TOFs, surface V_N sites of Ni/CeN were regarded as the active sites for the activation and adsorption of N_2 molecules, and then for further hydrogenation to produce NH_3, which could be determined from the concentration of the top layer $N_{lattice}$ of CeN. The amount of top layer $N_{lattice}$ was estimated from the unit cell of pure CeN to be 3.9×10^{14} cm^{-2}. The TOFs were then calculated from the reaction rate r_0, derived from the number of surface N atoms (eq 5):

$$TOFs = r_0 \cdot N_A / N_{surface\ N} \cdot S_{BET} \quad (5)$$

where r_0 is the reaction rate, N_A is Avogadro's constant, $N_{surface\ N}$ is the amount of top layer $N_{lattice}$ of CeN, and S_{BET} is the specific surface area of the catalyst. The surface of CeN was loaded with Ni NPs, which partially hindered the exposure of surface N atoms. Therefore, the TOFs obtained from this calculation method were underestimated.

Sample Characterization. The crystal structure was analyzed using X-ray diffraction (XRD; D8 Advance, Bruker) with Cu Kα

https://dx.doi.org/10.1021/jacs.0c06624
J. Am. Chem. Soc. XXXX, XXX, XXX−XXX

radiation (λ = 0.15418 nm). The samples were placed in Ar-filled capsules to protect them from air exposure. The morphology of the samples was evaluated using field-emission scanning electron microscopy (FE-SEM; JSM-7600F, JEOL) and the component elements were analyzed using energy dispersive X-ray spectroscopy (EDX; JED-2300, JEOL). Transmission electron microscopy (TEM) and high-angle annular dark-field scanning transmission electron microscopy (HAADF−STEM) images were obtained using an atomic resolution analytical electron microscope (JEM-ARM200F, JEOL) operated at an accelerating voltage of 200 kV. Raman spectra of the samples were measured with a spectrometer (HR-800, Horiba Jobin Yvon), using a laser with a wavelength of 457.4 nm. Auger electron spectroscopy (AES) was performed with 10 keV primary electrons using a scanning Auger nanoprobe system (PHI 710, Ulvac-Phi). Nitrogen sorption measurements (BELSORP-mini II, BEL) were applied to evaluate the Brunauer−Emmett−Teller (BET) surface areas of the catalysts. Temperature-programmed reduction with H_2 (H_2-TPR; BELCAT-A, BEL) was also conducted. Prior to measurements, the catalysts (0.1 g) were introduced into a quartz glass cell in an Ar-filled glovebox. The glass cell was then heated (10 °C·min^{-1}) in a stream of 4.8% H_2/Ar, and the H_2 consumption and gas products were monitored with a mass spectrometer (Bell Mass, BEL). Temperature-programmed desorption (TPD) of hydrogen (BELCAT-A, BEL) was performed using the same instrument for H_2-TPR. Prior to measurements, the catalysts (0.1 g) were introduced into a quartz glass cell in an Ar-filled glovebox and the glass cell was heated (10 °C·min^{-1}) in an Ar stream (50 mL·min^{-1}), and the concentration of H_2 was monitored with a thermal conductivity detector (TCD) and mass spectrometer (Bell Mass, BEL).

Isotope Experiment. Ammonia synthesis from $^{15}N_2$ isotope (98%) and H_2 was performed using a U-shaped glass reactor connected to a closed gas circulation system. The mixture of $^{15}N_2$ and H_2 gases (total pressure = 60 kPa, $^{15}N_2$:H_2 = 1:3) was introduced into the glass system, and the catalyst (0.2 g) was heated at different temperatures (Ni/CeN: 340 °C, CeN: 400 °C). The circulating gas was monitored using gas chromatography (GC; GC-8A, Shimadzu) with a Chromosorb 103 column to separate the NH_3 gas from the mixture, and the outlet gases from the chromatograph were also detected with a quadrupole mass spectrometer (M-101QA-TDM, Canon Anelva Corp.) and He was used as the carrier gas. The m/z = 2, 16, 17, 18, 28, 29, and 30 masses were monitored as a function of time to follow the reaction. The N_2 isotope exchange experiment was performed using a U-shaped glass reactor in connection with a closed gas circulation system. A mixture of $^{15}N_2$ and $^{14}N_2$, with total pressure of 20 kPa ($^{15}N_2$:$^{14}N_2$ = 1:4), was adsorbed on the catalyst at the reaction temperature until an adsorption equilibrium was reached. The circulating pump placed in the system removes diffusional and adsorption/desorption limitations. The circulating gas was monitored with a quadrupole mass spectrometer (M-101QA-TDM, Canon Anelva Corp.), and the mass-to-charge ratios (m/z) of 28, 29, and 30 were measured as a function of time.

Computational Calculations. All of the structural relaxation and electronic structure calculations were performed using density functional theory (DFT) as implemented in the Vienna Ab Initio Simulation Package (VASP).[43,44] The generalized gradient approximation (GGA) with the Perdew−Burke−Ernzerhof (PBE) functional[45] was adopted in the DFT calculations, and the core electrons were described using the projector augmented wave (PAW) method.[46,47] The PAW potentials used in this work were N, H, Ni, La, Ce_3, and Y_sv from the VASP distribution, where the Ce_3 potential is that where one 4f electron is kept frozen in the core and the valency of Ce is fixed to three. The Ce_3 potential was selected because nitrogen vacancy generation leads to inordinate electron doping into the Ce 4f bands with the DFT+U method using the Ce potential. Spin polarization in Ni was considered. First, the lattice parameters for bulk Ni and *Re*N were relaxed using Monkhorst−Pack grids of 20 × 20 × 20 and 12 × 12 × 12, respectively. An energy cutoff of 500 eV and total energy convergence of 10^{-6} eV were used to create the plane wave basis set. The *Re*N(001) surfaces, based on the optimized bulk lattice parameters, were selected for study because they were most favored for exposure. The *Re*N(001) surfaces were modeled by an 11 layer slab with a 4 × 4 lateral unit cell. A 20 Å thick vacuum region was set to prevent interaction between the slabs. The central 3 layers of atoms of the surface models were kept fixed to hold the characteristics of realistic surfaces, while the remainder of the unit cell was allowed to be fully relaxed during the geometry optimizations. A cutoff energy of 500 eV and a Monkhorst−Pack K-mesh setting of 3 × 3 × 1 were employed in the calculation for the *Re*N(001) surfaces. The vacuum level was confirmed as the energy level at which the electrostatic potential became constant. The atoms in the 4 bottom layers were then removed, and the atoms in the 4 top layers were relaxed for further V_N formation and TS calculations. The model of the Ni-loaded *Re*N surface was constructed by binding a Ni_8 cluster onto a *Re*N(001) surface. Here, the V_N site is located at the second nearest neighbor site (N[1]) with respect to Ni_8 cluster (Figure S23).

The nitrogen vacancy formation energy (E_{NV}) of the *Re*N(001) and Ni/*Re*N surfaces are defined as (eq 6):

$$E_{NV} = E_{tot}(V_N/\text{surface}) - E_{tot}(\text{surface}) + 1/2E_{tot}(N_2) \quad (6)$$

where $E_{tot}(V_N/\text{surface})$ is the total energy for the optimized surface nitrogen atom desorption configuration at different surfaces, $E_{tot}(\text{surface})$ is the total energy of the surface model, and $E_{tot}(N_2)$ is the total energy of an N_2 molecule.

The adsorption energies of X [$E_{ad}(X)$] (X represents H_2 or N_2) species on the surfaces are defined as (eq 7):

$$E_{ad}(X) = E_{tot}(X/\text{surface}) - E_{tot}(\text{surface}) - E_{tot}(X) \quad (7)$$

where $E_{tot}(X/\text{surface})$ is the total energy of the optimized X molecule/atom adsorption configuration, and $E_{tot}(X)$ is the total energy of an X molecule or atom. The TSs were searched using the climbing image-nudged elastic band (CI-NEB) method.[48] The energy and force convergence criteria were set to 10^{-6} eV and 0.05 eV·Å^{-1}, respectively. All molecules in the gas phase were relaxed in a box with dimensions of 20 × 20 × 20 Å^3.

■ ASSOCIATED CONTENT

Supporting Information

The Supporting Information is available free of charge at https://pubs.acs.org/doi/10.1021/jacs.0c06624.

Structural characterizations, catalytic activity data, and DFT calculation details including Figures S1−S23 and Tables S1−S7 (PDF)

■ AUTHOR INFORMATION

Corresponding Authors

Masaaki Kitano − *Materials Research Center for Element Strategy, Tokyo Institute of Technology, Midori-ku, Yokohama 226-8503, Japan; Precursory Research for Embryonic Science and Technology (PRESTO), Japan Science and Technology Agency (JST), Kawaguchi, Saitama 332-0012, Japan;* orcid.org/0000-0003-4466-7387; Email: kitano.m.aa@m.titech.ac.jp

Hideo Hosono − *Materials Research Center for Element Strategy, Tokyo Institute of Technology, Midori-ku, Yokohama 226-8503, Japan; International Center for Materials Nanoarchitectonics, National Institute for Materials Science, Tsukuba, Ibaraki 305-0044, Japan;* orcid.org/0000-0001-9260-6728; Email: hosono@mces.titech.ac.jp

Authors

Tian-Nan Ye − *Materials Research Center for Element Strategy, Tokyo Institute of Technology, Midori-ku, Yokohama 226-8503, Japan;* orcid.org/0000-0001-9039-8232

Sang-Won Park − *Materials Research Center for Element Strategy, Tokyo Institute of Technology, Midori-ku, Yokohama*

https://dx.doi.org/10.1021/jacs.0c06624
J. Am. Chem. Soc. XXXX, XXX, XXX−XXX

226-8503, Japan; International Center for Materials Nanoarchitectonics, National Institute for Materials Science, Tsukuba, Ibaraki 305-0044, Japan; orcid.org/0000-0002-2843-9803

Yangfan Lu − *Materials Research Center for Element Strategy, Tokyo Institute of Technology, Midori-ku, Yokohama 226-8503, Japan;* orcid.org/0000-0003-2084-9549

Jiang Li − *Materials Research Center for Element Strategy, Tokyo Institute of Technology, Midori-ku, Yokohama 226-8503, Japan*

Masato Sasase − *Materials Research Center for Element Strategy, Tokyo Institute of Technology, Midori-ku, Yokohama 226-8503, Japan*

Complete contact information is available at: https://pubs.acs.org/10.1021/jacs.0c06624

Author Contributions

#T.N.Y., S.W.P., and Y.L. contributed equally to this work.

Notes

The authors declare no competing financial interest.

■ ACKNOWLEDGMENTS

This work was supported by a grant from the Element Strategy Initiative to Form Core Research Center (No. JPMXP0112101001) of the Ministry of Education, Culture, Sports, Science and Technology of Japan (MEXT). A part of this work was supported by a PRESTO Grant (No. JPMJPR18T6) from the Japan Science and Technology Agency (JST) and Kakenhi Grants-in-Aid (Nos. 17H06153, JP19H05051, and JP19H02512) from the Japan Society for the Promotion of Science (JSPS). T. N. Ye is supported by a JSPS fellowship for International Research Fellows (No. P18361). Y. F. Lu is supported by a JSPS fellowship for young scientists (No. 18J00745). The authors thank Dr. Y. Sato (Tokyo Institute of Technology) for technical support with the Auger electron spectroscopy measurements.

■ REFERENCES

(1) Smil, V. Detonator of the population explosion. *Nature* **1999**, *400*, 415.

(2) Pool, A. J.; Lobkovsky, E.; Chirik, P. J. Hydrogenation and cleavage of dinitrogen to ammonia with a zirconium complex. *Nature* **2004**, *427*, 527−530.

(3) Gambarotta, S.; Scott, J. Multimetallic cooperative activation of N_2. *Angew. Chem., Int. Ed.* **2004**, *43*, 5298−5308.

(4) Honkala, K.; Hellman, A.; Remediakis, I. N.; Logadottir, A.; Carlsson, A.; Dahl, S.; Christensen, C. H.; Nørskov, J. K. Ammonia synthesis from first-principles calculations. *Science* **2005**, *307*, 555−558.

(5) Erisman, J. W.; Sutton, M. A.; Galloway, J.; Klimont, Z.; Winiwarter, W. How a century of ammonia synthesis changed the world. *Nat. Geosci.* **2008**, *1*, 636−639.

(6) Chen, J. G.; Crooks, R. M.; Seefeldt, L. C.; Bren, K. L.; Bullock, R. M.; Darensbourg, M. Y.; Holland, P. L.; Hoffman, B.; Janik, M. J.; Jones, A. K.; Kanatzidis, M. G.; King, P.; Lancaster, K. M.; Lymar, S. V.; Pfromm, P.; Schneider, W. F.; Schrock, R. R. Beyond fossil fuel-driven nitrogen transformations. *Science* **2018**, *360*, eaar6611.

(7) Licht, S.; Cui, B.; Wang, B.; Li, F.; Lau, J.; Liu, S. Ammonia synthesis by N_2 and steam electrolysis in molten hydroxide suspensions of nanoscale Fe_2O_3. *Science* **2014**, *345*, 637−640.

(8) Hao, Y.; Guo, Y.; Chen, L.; Shu, M.; Wang, X.; Bu, T.; Gao, W.; Zhang, N.; Su, X.; Feng, X.; Zhou, J.; Wang, B.; Hu, C.; Yin, A.; Si, R.; Zhang, Y.; Yan, C. Promoting nitrogen electro-reduction to ammonia with bismuth nanocrystals and potassium cations in water. *Nat. Catal.* **2019**, *2*, 448−456.

(9) Zhu, D.; Zhang, L. H.; Ruther, R. E.; Hamers, R. J. Photo-illuminated diamond as a solid-state source of solvated electrons in water for nitrogen reduction. *Nat. Mater.* **2013**, *12*, 836−841.

(10) Li, H.; Shang, J.; Ai, Z. H.; Zhang, L. Z. Efficient visible light nitrogen fixation with BiOBr nanosheets of oxygen vacancies on the exposed {001} facets. *J. Am. Chem. Soc.* **2015**, *137*, 6393−6399.

(11) Tompsett, D. A.; Parker, S. C.; Islam, M. S. Rutile (β-)MnO_2 surfaces and vacancy formation for high electrochemical and catalytic performance. *J. Am. Chem. Soc.* **2014**, *136*, 1418−1426.

(12) Jeen, H.; Bi, Z.; Choi, W.; Chisholm, M. F.; Bridges, C. A.; Paranthaman, M. P.; Lee, H. Orienting oxygen vacancies for fast catalytic reaction. *Adv. Mater.* **2013**, *25*, 6459−6463.

(13) Zhao, D.; Chen, Z.; Yang, W.; Liu, S.; Zhang, X.; Yu, Y.; Cheong, W.; Zheng, L.; Ren, F.; Ying, G.; Cao, X.; Wang, D.; Peng, Q.; Wang, G.; Chen, C. MXene (Ti_3C_2) vacancy-confined single-atom catalyst for efficient functionalization of CO_2. *J. Am. Chem. Soc.* **2019**, *141*, 4086−4093.

(14) Mars, P.; van Krevelen, D. W. Oxidations carried out by means of vanadium oxide catalysts. *Chem. Eng. Sci.* **1954**, *3*, 41−59.

(15) Campbell, C. T.; Peden, C. H. F. Oxygen vacancies and catalysis on ceria surfaces. *Science* **2005**, *309*, 713−714.

(16) Esch, F.; Fabris, S.; Zhou, L.; Montini, T.; Africh, C.; Fornasiero, P.; Comelli, G.; Rosei, R. Electron localization determines defect formation on ceria substrates. *Science* **2005**, *309*, 752−755.

(17) Lawrence, N. J.; Brewer, J. R.; Wang, L.; Wu, T.; Wells-Kingsbury, J.; Ihrig, M. M.; Wang, G.; Soo, Y.; Mei, W.; Cheung, C. Defect engineering in cubic cerium oxide nanostructures for catalytic oxidation. *Nano Lett.* **2011**, *11*, 2666−2671.

(18) Hargreaves, J. S. J. Nitrides as ammonia synthesis catalysts and as potential nitrogen transfer reagents. *Appl. Petrochem. Res.* **2014**, *4*, 3−10.

(19) Zeinalipour-Yazdi, C. D.; Hargreaves, J. S. J.; Catlow, C. R. A. Nitrogen activation in a Mars−van Krevelen mechanism for ammonia synthesis on Co_3Mo_3N. *J. Phys. Chem. C* **2015**, *119*, 28368−28376.

(20) Laassiri, S.; Zeinalipour-Yazdi, C. D.; Catlow, C. R. A.; Hargreaves, J. S. J. The potential of manganese nitride based materials as nitrogen transfer reagents for nitrogen chemical looping. *Appl. Catal., B* **2018**, *223*, 60−66.

(21) Kitano, M.; Inoue, Y.; Yamazaki, Y.; Hayashi, F.; Kanbara, S.; Matsuishi, S.; Yokoyama, T.; Kim, S. W.; Hara, M.; Hosono, H. Ammonia synthesis using a stable electride as an electron donor and reversible hydrogen store. *Nat. Chem.* **2012**, *4*, 934−940.

(22) Kitano, M.; Kanbara, S.; Inoue, Y.; Kuganathan, N.; Sushko, P. V.; Yokoyama, T.; Hara, M.; Hosono, H. Electride support boosts nitrogen dissociation over ruthenium catalyst and shifts the bottleneck in ammonia synthesis. *Nat. Commun.* **2015**, *6*, 6731.

(23) Kitano, M.; Inoue, Y.; Ishikawa, H.; Yamagata, K.; Nakao, T.; Tada, T.; Matsuishi, S.; Yokoyama, T.; Hara, M.; Hosono, H. Essential role of hydride ion in ruthenium-based ammonia synthesis catalysts. *Chem. Sci.* **2016**, *7*, 4036−4043.

(24) Kitano, M.; Inoue, Y.; Sasase, M.; Kishida, K.; Kobayashi, Y.; Nishiyama, K.; Tada, T.; Kawamura, S.; Yokoyama, T.; Hara, M.; Hosono, H. Self-organized ruthenium-barium core-shell nanoparticles on a mesoporous calcium amide matrix for efficient low temperature ammonia synthesis. *Angew. Chem., Int. Ed.* **2018**, *57*, 2648−2652.

(25) Inoue, Y.; Kitano, M.; Kishida, K.; Abe, H.; Niwa, Y.; Sasase, M.; Fujita, Y.; Ishikawa, H.; Yokoyama, T.; Hara, M.; Hosono, H. Efficient and stable ammonia synthesis by self-organized flat Ru nanoparticles on calcium amide. *ACS Catal.* **2016**, *6*, 7577−7584.

(26) Kanbara, S.; Kitano, M.; Inoue, Y.; Yokoyama, T.; Hara, M.; Hosono, H. Mechanism switching of ammonia synthesis over Ru-loaded electride catalyst at metal-insulator transition. *J. Am. Chem. Soc.* **2015**, *137*, 14517−14524.

(27) Wang, P. K.; Chang, F.; Gao, W. B.; Guo, J. P.; Wu, G. T.; He, T.; Chen, P. Breaking scaling relations to achieve low-temperature ammonia synthesis through LiH-mediated nitrogen transfer and hydrogenation. *Nat. Chem.* **2017**, *9*, 64−70.

(28) Chang, F.; Guan, Y. Q.; Chang, X. H.; Guo, J. P.; Wang, P. K.; Gao, W. B.; Wu, G. T.; Zheng, J.; Li, X. G.; Chen, P. Alkali and

alkaline earth hydrides-driven N_2 activation and transformation over Mn nitride catalyst. *J. Am. Chem. Soc.* **2018**, *140*, 14799−14806.
(29) Gao, W. B.; Wang, P. K.; Guo, J. P.; Chang, F.; He, T.; Wang, Q. R.; Wu, G. T.; Chen, P. Barium hydride-mediated nitrogen transfer and hydrogenation for ammonia synthesis: A case study of cobalt. *ACS Catal.* **2017**, *7*, 3654−3661.
(30) Kitano, M.; Kujirai, J.; Ogasawara, K.; Matsuishi, S.; Tada, T.; Abe, H.; Niwa, Y.; Hosono, H. Low-temperature synthesis of perovskite oxynitride-hydrides as ammonia synthesis catalysts. *J. Am. Chem. Soc.* **2019**, *141*, 20344−20353.
(31) Kobayashi, Y.; Hernandez, O. J.; Sakaguchi, T.; Yajima, T.; Roisnel, T.; Tsujimoto, Y.; Morita, M.; Noda, Y.; Mogami, Y.; Kitada, A.; Ohkura, M.; Hosokawa, S.; Li, Z. F.; Hayashi, K.; Kusano, Y.; Kim, J. E.; Tsuji, N.; Fujiwara, A.; Matsushita, Y.; Yoshimura, K.; Takegoshi, K.; Inoue, M.; Takano, M.; Kageyama, H. An oxyhydride of $BaTiO_3$ exhibiting hydride exchange and electronic conductivity. *Nat. Mater.* **2012**, *11*, 507−511.
(32) Kobayashi, Y.; Tang, Y.; Kageyama, T.; Yamashita, H.; Masuda, N.; Hosokawa, S.; Kageyama, H. Titanium-based hydrides as heterogeneous catalysts for ammonia synthesis. *J. Am. Chem. Soc.* **2017**, *139*, 18240−18246.
(33) Tang, Y.; Kobayashi, Y.; Masuda, N.; Uchida, Y.; Okamoto, H.; Kageyama, T.; Hosokawa, S.; Loyer, F.; Mitsuhara, K.; Yamanaka, K.; Tamenori, Y.; Tassel, C.; Yamamoto, T.; Tanaka, T.; Kageyama, H. Metal-dependent support effects of oxyhydride-supported Ru, Fe, Co Catalysts for ammonia synthesis. *Adv. Energy Mater.* **2018**, *8*, 1801772.
(34) Ye, T. N.; Park, S. W.; Lu, Y.; Li, J.; Sasase, M.; Kitano, M.; Tada, T.; Hosono, H. Vacancy-enabled N_2 activation for ammonia synthesis on an Ni-loaded catalyst. *Nature* **2020**, *583*, 391−395.
(35) Gao, W.; Guo, J.; Wang, P.; Wang, Q.; Chang, F.; Pei, Q.; Zhang, W.; Liu, L.; Chen, P. Production of ammonia via a chemical looping process based on metal imides as nitrogen carriers. *Nat. Energy* **2018**, *3*, 1067−1075.
(36) Kojima, R.; Aika, K. Cobalt molybdenum bimetallic nitride catalysts for ammonia synthesis: Part 2. Kinetic study. *Appl. Catal., A* **2001**, *218*, 121−128.
(37) Bion, N.; Can, F.; Cook, J.; Hargreaves, J. S. J.; Hector, A. L.; Levason, W.; McFarlane, A. R.; Richard, M.; Sardar, K. The role of preparation route upon the ambient pressure ammonia synthesis activity of Ni_2Mo_3N. *Appl. Catal., A* **2015**, *504*, 44−50.
(38) Inoue, Y.; Kitano, M.; Tokunari, M.; Taniguchi, T.; Ooya, K.; Abe, H.; Niwa, Y.; Sasase, M.; Hara, M.; Hosono, H. Direct activation of cobalt catalyst by $12CaO{\cdot}7Al_2O_3$ electride for ammonia synthesis. *ACS Catal.* **2019**, *9*, 1670−1679.
(39) Gong, Y. T.; Wu, J. Z.; Kitano, M.; Wang, J. J.; Ye, T. N.; Li, J.; Kobayashi, Y.; Kishida, K.; Abe, H.; Niwa, Y.; Yang, H. S.; Tada, T.; Hosono, H. Ternary intermetallic LaCoSi as a catalyst for N_2 activation. *Nat. Catal.* **2018**, *1*, 178−185.
(40) Wu, J.; Li, J.; Gong, Y.; Kitano, M.; Inoshita, T.; Hosono, H. Intermetallic electride catalyst as a platform for ammonia synthesis. *Angew. Chem., Int. Ed.* **2019**, *58*, 825−829.
(41) Balasubramanian, K.; Khare, S. V.; Gall, D. Energetics of point defects in rocksalt structure transition metal nitrides: Thermodynamic reasons for deviations from stoichiometry. *Acta Mater.* **2018**, *159*, 77−88.
(42) Lu, Y.; Li, J.; Ye, T. N.; Kobayashi, Y.; Sasase, M.; Kitano, M.; Hosono, H. Synthesis of rare-earth-based metallic electride nanoparticles and their catalytic applications to selective hydrogenation and ammonia synthesis. *ACS Catal.* **2018**, *8*, 11054−11058.
(43) Kresse, G.; Furthmüller, J. Efficient iterative schemes for ab initio total-energy calculations using a plane-wave basis set. *Phys. Rev. B: Condens. Matter Mater. Phys.* **1996**, *54*, 11169−11186.
(44) Kresse, G.; Joubert, D. From ultrasoft pseudopotentials to the projector augmented-wave method. *Phys. Rev. B: Condens. Matter Mater. Phys.* **1999**, *59*, 1758−1775.
(45) Perdew, J. P.; Burke, K.; Ernzerhof, M. Generalized gradient approximation made simple. *Phys. Rev. Lett.* **1996**, *77*, 3865−3868.
(46) Blöchl, P. E. Projector augmented-wave method. *Phys. Rev. B: Condens. Matter Mater. Phys.* **1994**, *50*, 17953−17979.
(47) Perdew, J. P.; Burke, K.; Ernzerhof, M. Generalized gradient approximation made simple. [Phys. Rev. Lett. 1996, 77, 3865]. *Phys. Rev. Lett.* **1997**, *78*, 1396−1396.
(48) Henkelman, G.; Jónsson, H. Improved tangent estimate in the nudged elastic band method for finding minimum energy paths and saddle points. *J. Chem. Phys.* **2000**, *113*, 9978−9985.

https://dx.doi.org/10.1021/jacs.0c06624
J. Am. Chem. Soc. XXXX, XXX, XXX−XXX